

Influence of forward and multiple light scatter on the measurement of beam attenuation in highly scattering marine environments

Jacek Piskozub, Dariusz Stramski, Eric Terrill, and W. Kendall Melville

Using three-dimensional Monte Carlo radiative transfer simulations, we examine the effect of beam transmissometer geometry on the relative error in the measurement of the beam-attenuation coefficient in an aquatic environment characterized by intense light scattering, especially within submerged bubble clouds entrained by surface-wave breaking. We discuss the forward-scattering error associated with the detection of photons scattered at small angles ($<1^\circ$) and the multiple-scattering error associated with the detection of photons scattered more than once along the path length of the instrument. Several scattering phase functions describing bubble clouds at different bubble void fractions in the water are considered. Owing to forward-scattering error, a beam-attenuation meter (beam transmissometer) with a half-angle of receiver acceptance of 1.0° and a path length of 0.1 m can underestimate the true beam attenuation within the bubble cloud by more than 50%. For bubble clouds with a beam attenuation of as much as 100 m^{-1} , the multiple-scattering error is no more than a few percent. These results are compared with simulations for some example phase functions that are representative of other scattering regimes found in natural waters. The forward-scattering error for the Petzold phase function of turbid waters is 16% for a typical instrument geometry, whereas for the Henyey–Greenstein phase function with the asymmetry parameter of 0.7 and 0.9 the error range is 8–28%. © 2004 Optical Society of America

OCIS codes: 010.4450, 120.4640, 010.7340.

1. Introduction

Spectral beam-attenuation coefficient $c(\lambda)$, where λ is the wavelength of light in vacuum, is an important inherent optical property (IOP) of natural aquatic media^{1,2} that has long been measured routinely *in situ*.^{3–5} The beam-attenuation meter is conceptually simpler than devices for measuring other IOPs. This is so partly because the beam attenuation reflects the cumulative influence of the scattering and absorption properties of the medium, such that the value of $c(\lambda)$ is the sum of absorption coefficient $a(\lambda)$ and scattering coefficient $b(\lambda)$. It is extremely difficult to make precise measurements of absorption coefficient $a(\lambda)$ in aquatic environments. In principle,

all the scattered radiation should be collected when direct measurements are made with instruments such as reflective tube meters.⁶ In indirect determinations of absorption from irradiance measurements, small differences in irradiance must be accurately measured.⁷ Making direct measurements of scattering coefficient $b(\lambda)$ is also difficult, because the light scattered into all directions, including small-angle forward directions near 0° and backward directions near 180° , has to be accurately measured.

At first glance, the determination of the beam attenuation from measurements of the intensity of the primary unscattered beam at a known distance from the light source might appear to be a relatively simple task. In practice, the receiver of the beam-attenuation meter (usually referred to as the beam transmissometer) will have a finite acceptance angle, leading to the detection of small-angle forward light scatter. It has long been recognized that forward-scattering error makes it impossible to measure accurately the true beam-attenuation coefficient.^{8,9} To minimize the error that is due to forward scattering the receiver acceptance angle should be only slightly larger than the divergence of the source beam

J. Piskozub (piskozub@iopan.gda.pl) is with the Institute of Oceanography, Polish Academy of Sciences, Powstańców Warszawy 55, Sopot 81-712, Poland. D. Stramski, E. Terrill, and W. K. Melville are with the Marine Physical Laboratory, Scripps Institution of Oceanography, University of California, San Diego, La Jolla, California 92093-0238.

Received 21 November 2003.

0003-6935/04/244723-09\$15.00/0

© 2004 Optical Society of America

and the collecting surface area of the receiver should be as small as possible while encompassing the beam.

Another problem of the beam-attenuation measurement is related to the selection of the appropriate path length. The path length must be long enough to produce a measurable loss of beam intensity within the sensitivity of the receiving system. The definition of the beam-attenuation coefficient, however, requires measurement under single-scattering conditions. The longer the path length, the greater the probability that multiply scattered photons will be detected, which lead to error. The path length in the beam transmissometers used for measurements in the ocean is typically 0.1–1 m. This is usually appropriate in terms of both producing a measurable signal and minimizing the error that is due to multiple scattering. However, in a medium that has high scattering, a path length that is long enough to cause a significant loss of beam intensity may also lead to multiple scattering of photons within the beam, especially if the scattering phase function (*i.e.*, the angular distribution of the scattered photons) is strongly peaked in forward directions. The most representative example of such a medium within a marine environment is submerged clouds of air bubbles produced by surface-wave breaking. Bubble clouds in ocean surface layers may be an important factor in influencing light scattering and spectral ocean reflectance and therefore may create significant errors in remotely sensed data products.^{10,11} Bubbles are characterized by high values of single-scattering albedo (high probability of photon survival) because light absorption by bubbles, even if they are covered with organic coating, is virtually negligible.¹² The scattering phase function of bubble populations is highly peaked in the forward directions owing to the relatively large size of the bubbles (~10 to ~1000 μm) relative to visible optical wavelengths.^{10,11} Therefore, for determinations of the beam-attenuation coefficient within a collection of bubbles (typically made near the ocean surface during sea states characterized by active wave breaking), it is important to know the values of both the multiple-scattering error and the small-angle forward-scattering error. The objective of this study is to estimate the effect of these errors on the accuracy of the beam-attenuation measurement. Our approach is based on three-dimensional Monte Carlo simulations of radiative transfer.

2. Description of Model Computations

A typical beam transmissometer utilizes an almost parallel (usually slightly divergent) light beam coming from a source window and propagating toward a circular receiver window. Both windows are centered on and are perpendicular to the beam axis. The viewing angle of the receiver is limited because an ultimate goal is to detect only the unscattered photons of the primary beam. For the same reason it is prudent to reduce the size of the collecting surface of the receiver such that it is only slightly larger than the beam size.

We performed Monte Carlo simulations of radiative transfer for the geometry of a typical beam transmissometer, such as C-Star or ac-9 (WetLabs, Inc), that is used in oceanographic measurements. In these simulations the essential parameters that characterize the instrument receiver and path length were varied to some extent. The Monte Carlo code used in this study had previously been applied to the study of the effects of instrument self-shading on underwater light-field measurements,¹³ scattering error of a reflective absorption tube,¹⁴ and scattering error in spectrophotometric measurements of light absorption.¹⁵ In the version of the code used in this study, photons are generated at a random starting position within a circle simulating the source beam that enters the modeled environment. For the beam with a nonzero half-angle of divergence θ_{beam} , the initial directions of photons defined by the polar angle (measured from the beam axis) and the azimuth angle are randomly selected. The photons are subsequently traced in three-dimensional space until they reach the receiver, are absorbed, or leave the modeled environment. The collecting surface of the receiver is modeled as a circle of radius r centered about and perpendicular to the beam axis. The receiver is placed a distance d from the light source. This distance is referred to as the path length of the modeled instrument. The photons that reach the receiver are detected if the polar angle of the photon direction is smaller than the assumed half-angle of the receiver acceptance, θ_a .

The Monte Carlo code allowed us to use several receiver radii and acceptance angles with one set of source photons, making the simulations efficient. Unless stated otherwise, the standard set of parameters that characterize the modeled instrument in our simulations was as follows: an initial beam radius of 0.001 m, a half-angle of beam divergence of 0.8°, a half-angle of receiver acceptance of 1°, a receiver radius of 0.0095 m, and a path length of 0.1 m. The measured value of the beam-attenuation coefficient, c_{meas} [m^{-1}], was calculated from the operational definition of the coefficient according to

$$c_{\text{meas}} = \frac{1}{d} \ln \frac{\Phi_0}{\Phi}, \quad (1)$$

where Φ_0 is the radiant power (or number of photons) at the light source (or incident upon the water sample), Φ is the radiant power incident upon (or measured by) the virtual receiver, with its position, size, and acceptance angle taken in account, and d is the instrument's path length.

A unique attribute of the IOPs that are used as input to these radiative transfer simulations is the broad range of scattering coefficient b that is chosen. Whereas studies of ocean optics usually deal with typical oceanic values of b that range from $\sim 10^{-2}$ to $\sim 1 \text{ m}^{-1}$, recent research indicates that dense bubble clouds near the ocean surface during elevated sea states will have void fractions that exceed 10^{-3} and an optical scattering coefficient that can be greater

than 10 m^{-1} .¹¹ Motivated by the need to understand the propagation of light through these highly scattering media, we extended values for b to represent those conditions that might be found within dense collections of bubbles. For the studies described, we chose b to range from 0.2 m^{-1} to very high value of 1000 m^{-1} .

Scattering phase function $\tilde{\beta}(\psi, \lambda) [\text{sr}^{-1}]$ is an additional IOP input required for radiative transfer simulations. This function describes the angular distribution of the scattered photons normalized to the total scattering coefficient²:

$$\tilde{\beta}(\lambda, \psi) = \frac{\beta(\psi, \lambda)}{b(\lambda)}, \quad (2)$$

where ψ is the scattering angle between the direction of the incident beam and the direction of scattered photons and $\beta(\psi, \lambda)$ is the spectral volume scattering function [$\text{m}^{-1} \text{ sr}^{-1}$]. The values of ψ are 0° – 180° . Function $\beta(\psi, \lambda)$ represents the spectral radiant intensity [$\text{W sr}^{-1} \text{ nm}^{-1}$] scattered into direction ψ per unit incident irradiance [$\text{W m}^{-2} \text{ nm}^{-1}$] per unit volume of water [m^3] illuminated by the incident beam. Note that integrating $\beta(\psi, \lambda)$ over all scattering directions yields $b(\lambda)$ and that integrating $\tilde{\beta}(\psi, \lambda)$ yields 1.

Few descriptions of phase functions dominated by scattering by bubble populations generated by wave breaking exist in the literature.^{10,16} This could be so in part because of our inability to measure bubble phase functions within the rigors of oceanic conditions when surface waves are breaking and with a temporal resolution that would capture the transitory nature of bubbles. As a result of these difficulties, we rely on computing the phase functions for bubble populations by using the Mie scattering theory for homogeneous spheres. For this purpose we have used the code given by Bohren and Huffman.¹⁷ Because of the temporal nature of ocean bubble size distributions, we chose representative bubble size distributions, which are characterized by their total void fraction, with which to compute a range of phase functions that span bubble densities from 10^{-9} to 10^{-3} . These size distributions were obtained from *in situ* measurements with a sound velocimeter with a broadband acoustic pulse (2–140 kHz), which permitted the estimation of size distributions over a range of bubble radii from 20 to 1600 μm .¹⁸ This range has been shown to span the majority of the sizes of optically significant bubbles.¹¹ As input to the Mie computations, six different bubble size distributions were determined by ensemble averaging of many size distributions that had been binned over void fractions that spanned order-of-magnitude ranges: from 10^{-9} to 10^{-8} , from 10^{-8} to 10^{-7} , from 10^{-7} to 10^{-6} , from 10^{-6} to 10^{-5} , from 10^{-5} to 10^{-4} , and from 10^{-4} to 10^{-3} . The Mie calculations of bubble phase functions were made for each of these six size distributions with the assumption that the real part of the refractive index of bubbles (relative to water) is 1.34^{-1} and that bubbles are clean, with no surface

coating and no absorption. The calculations were made for a wavelength of light of 550 nm, but the results are applicable over a broad range of visible wavelengths, as the phase functions for bubbles have a weak spectral dependence owing to the relatively large bubble sizes. The calculated phase functions are based on the assumption that scattering is azimuthally symmetric about the incident direction of an unpolarized light beam.

In addition to the phase functions of bubbles, the Monte Carlo simulations were also made with the one-term Henyey–Greenstein (HG) phase function¹⁹ with different values of asymmetry parameter g as well as with the Petzold phase function obtained from measurements in turbid waters of San Diego Harbor.²⁰ The inclusion of these other phase functions in our set of simulations will provide an indication of the sensitivity of the results to non-bubble-dominated phase functions. The Petzold phase function from San Diego Harbor is assumed to be dominated by suspended solid particles. The HG phase function, $\tilde{\beta}_{\text{HG}}(\psi, \lambda)$, is used because of its mathematical simplicity and historical popularity in radiative transfer calculations in astrophysics and environmental optics.^{21,22} For any given wavelength λ , this function is defined as

$$\tilde{\beta}_{\text{HG}}(g, \psi) = \frac{1}{4\pi} \frac{1 - g^2}{(1 + g^2 - 2g \cos \psi)^{3/2}}. \quad (3)$$

As the value of asymmetry parameter g approaches 1, the $\tilde{\beta}_{\text{HG}}$ function becomes strongly peaked in the forward direction. For $g = 0$, $\tilde{\beta}_{\text{HG}}$ yields isotropic scattering. The most suitable values of g for atmospheric aerosols and oceanic particles are of the order of 0.7–0.9, although fitting the actual phase functions of natural particulate assemblages with a one-term HG function is known to have shortcomings.^{23,24}

Figure 1 shows that the phase functions of bubbles are similar for all void fractions considered, except for the scattering angles close to 0° and 180° . To facilitate the illustration of the differences in the forward- and backward-scattering directions, we present a cumulative phase function, which represents an integral from 0° to a given scattering angle as a function of scattering angle, in Fig. 2. All the bubble phase functions are strongly peaked in the forward directions, although the relative amount of forward scattering is dependent on the void fraction. For the void fraction range 10^{-9} – 10^{-8} , 50% of all the scattered intensity is contained within the forward-scattering angles from 0° to 1° . For the highest void fraction considered (10^{-4} – 10^{-3}), 80% of the scattered intensity goes into this narrow range of forward directions. In addition, Fig. 2 shows that the forward scattering is much more pronounced for the bubble phase functions than for the Petzold and HG functions, even for $g = 0.9$. The differences in phase function among different bubble void fractions is a result of the bubble size distribution that evolves as a function of time that was once introduced by wave

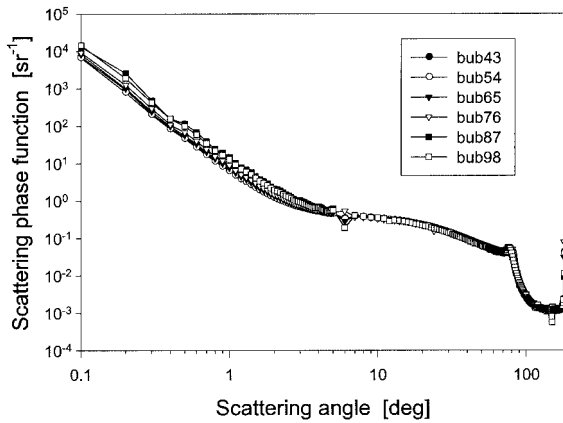


Fig. 1. Scattering phase functions for bubble populations calculated from Mie theory by use of bubble size distributions measured acoustically under breaking waves at several void fractions. The bubble phase functions for various void fraction ranges are written here and below as bub xy , where x and y define the void fraction range from 10^{-x} to 10^{-y} . The Mie calculations were made for $\lambda = 550$ nm.

breaking. The physics that governs the evolution of the bubble size distribution is a complicated interplay among bubble rise speed, gas dissolution, and turbulent mixing, which results in the presence of fewer large bubbles as the void fraction decreases.²⁵ As a result, the optical phase function becomes less peaked in the forward direction as the bubble void fraction decreases, and smaller bubbles dominate the scattering.

Monte Carlo simulations also require an input that characterizes the absorption properties of the medium. Most of our simulations were made with the assumption that the absorption coefficient has a relatively small value associated just with pure seawater. In such a case we have taken the absorption coefficient of pure seawater for the wavelength of 550 nm, which is 0.0565 m^{-1} .²⁶ Such an assumption about small or negligible absorption reflects our main interest in a medium, such as dense bubble clouds in surface ocean, with high scattering and with a high scattering-to-absorption ratio. However, we also made an additional set of Monte Carlo simulations in which we specifically addressed the possible effects of absorption on forward-scattering and multiple-scattering errors in the beam-attenuation measurements. In these simulations the range of the absorption coefficient was extended to the very high value of 20 m^{-1} .

All the Monte Carlo calculations were made for 10×10^6 photons for each set of input IOPs. We do not show the results for the situations when the input IOPs resulted in fewer than 100 photons detected by the virtual instrument.

3. Results and Discussion

The relative error of the beam-attenuation measurement can be defined as $c_{\text{meas}}/c_{\text{true}} - 1$, where c_{meas} is the measured beam-attenuation coefficient as calculated from Eq. (1) for a given set of parameters that

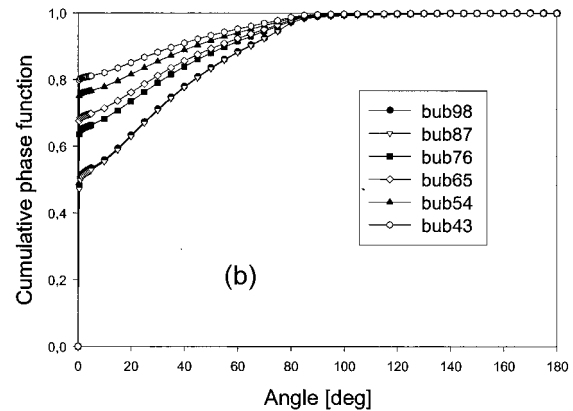
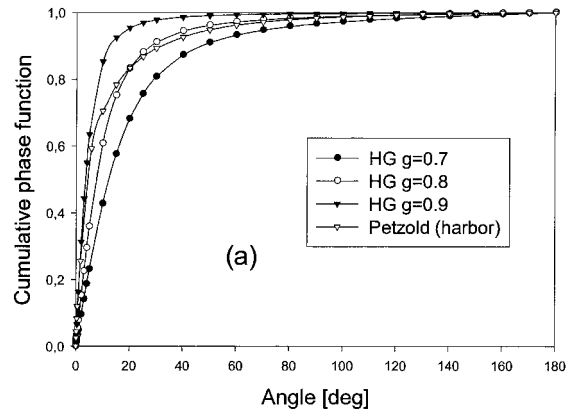


Fig. 2. Comparison of the cumulative scattering phase functions for (a) bubble populations at a number of void fraction ranges (see text and Fig. 1 for explanation) with (b) the Petzold cumulative phase function from San Diego Harbor and the HG cumulative phase functions for asymmetry parameter $g = 0.7, 0.8, 0.9$.

simulate the beam transmissometer instrument and c_{true} is the true beam-attenuation value used as input to the Monte Carlo calculations. In nearly all simulations made in this study c_{meas} underestimates c_{true} , so the relative error $c_{\text{meas}}/c_{\text{true}} - 1$ has a negative value. Below, we present the error values expressed as $1 - c_{\text{meas}}/c_{\text{true}}$ rather than as $c_{\text{meas}}/c_{\text{true}} - 1$, so the underestimation error is expressed simply by a positive value rather than by a negative value.

Figures 3 and 4 show $1 - c_{\text{meas}}/c_{\text{true}}$ as a function of c_{true} for instrument path lengths d of 0.1 and 0.25 m, respectively, assuming the HG phase functions. Other parameters of the modeled instrument were standard as defined above. Two features that can be seen from Fig. 3 and 4 deserve particular emphasis. First, the values of $1 - c_{\text{meas}}/c_{\text{true}}$ do not equal 0 even for small values of c_{true} , which implies a measurement error even in the single-scattering regime that is defined approximately by the condition that optical thickness $c_{\text{true}} d$ is smaller than 0.3.²¹ This is the forward-scattering error caused by the finite acceptance angle of the instrument receiver, which results in collecting some of the forward-scattered light. An ideal beam transmissometer should have an infinitely small acceptance angle, as the instrument is intended to collect only the unscat-

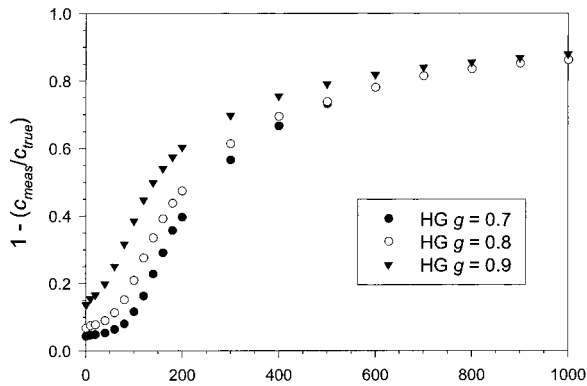


Fig. 3. Measurement error expressed as $1 - c_{\text{meas}}/c_{\text{true}}$ as a function of true beam attenuation c_{true} . The measured beam attenuation coefficient, c_{meas} , is calculated from the Monte Carlo radiative transfer model of the beam transmissometer, and the true beam attenuation, c_{true} , is used as input to the Monte Carlo model. The modeled instrument has a path length of 0.1 m, an initial beam radius of 0.001 m, a half-angle of beam divergence of 0.8° , a half-angle of receiver acceptance of 1° , and a receiver radius of 0.0095 m. The Monte Carlo simulations were made for the HG phase functions with asymmetry parameter $g = 0.7, 0.8, 0.9$.

tered photons of the primary (source) beam. However, diffraction effects and the fact that the source beam is always characterized by some degree of divergence make it impossible to satisfy the requirements of an ideal instrument. We note that the relative error values in Fig. 3 and 4 are similar for similar optical depths (defined as $c \times d$), which suggests that these results may be used for estimating attenuation errors for instruments with different path lengths.

Second, an underestimation error of the measurement increases with increasing true attenuation (or scattering) coefficient owing to multiple scattering. This means that the detected radiant power decreases with increasing attenuation more slowly than would be expected if no multiple scattering existed. This is so because each photon may be ultimately lost from the beam only once, whereas not every scattering event makes the photons leave the trajectories accepted by the receiver. Note that either of two

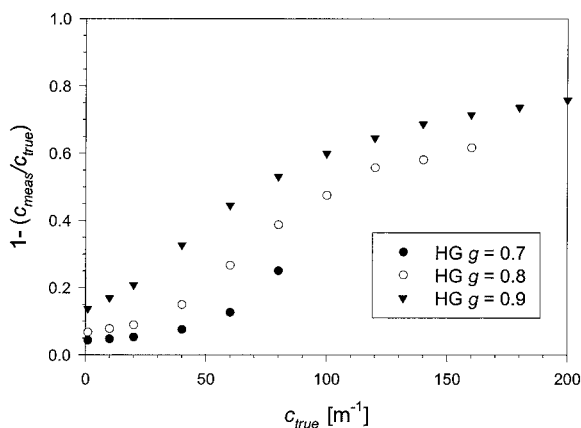


Fig. 4. Same as Fig. 3 but for instrument path length $d = 0.25$ m.

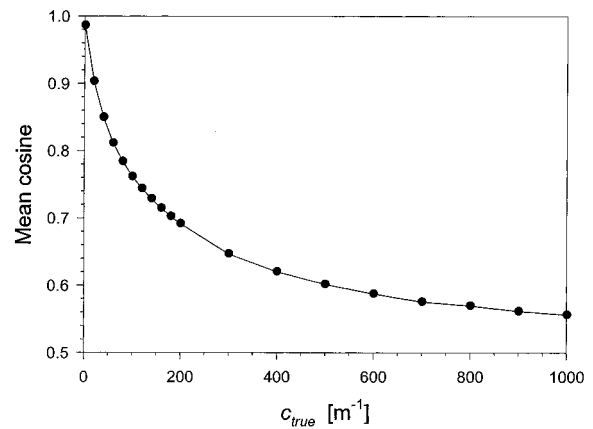


Fig. 5. Mean cosine of the light field relative to the beam axis produced by photons within the plane containing the collecting area of the receiver. The modeled instrument has a path length of 0.1 m, an initial beam radius of 0.001 m, and a half-angle of beam divergence of 0.8° . The parameters of the receiver itself are irrelevant to the results presented, as all the photons (both detected and undetected) reaching the plane of the receiver contribute to the mean cosine. The calculations were made for the HG scattering phase function with $g = 0.8$.

mechanisms can be responsible for photons that leave these trajectories: First, the scattered photons may not hit the collecting area of the receiver, and second, the scattered photons may hit the collecting area of the receiver at an angle greater than the acceptance angle of the receiver. The multiple-scattering error is associated with the fact that there must always exist some photons that are scattered away from the receiver by the first scattering event and then scattered back toward the receiver by subsequent scattering event(s). Such photons are detected by the receiver only because they are scattered more than once. This phenomenon suggests that there exists a value of scattering coefficient b above which the light field reaches an asymptotic radiance distribution along the instrument's path length. Further increase of b would not cause any further scattering-induced changes in the distribution of photon angles with respect to the beam axis. With no such changes, no further decrease of radiant power reaching the receiver would be detected, and in consequence one would expect to see a plateau in the plot of $1 - c_{\text{meas}}/c_{\text{true}}$ versus c_{true} . It seems that for the results presented in Fig. 3 this plateau associated with the asymptotic field conditions is reached for $c_{\text{true}} > 400 \text{ m}^{-1}$, which corresponds to an optical thickness of 40, given a path length of 0.1 m. An optical thickness greater than 40 should be sufficient for approaching these conditions.² However, a slow increase in $1 - c_{\text{meas}}/c_{\text{true}}$ under conditions of asymptotic light is still possible (see Fig. 3 for $c_{\text{true}} > 400 \text{ m}^{-1}$), which appears to be caused at least in part by photons' being scattered beyond the receiver's acceptance radius. Figure 5 shows the mean cosine of the light field² produced by photons at the receiver window as a function of c_{true} (note that c_{true} here is equivalent to the true scattering coefficient, b_{true}). The

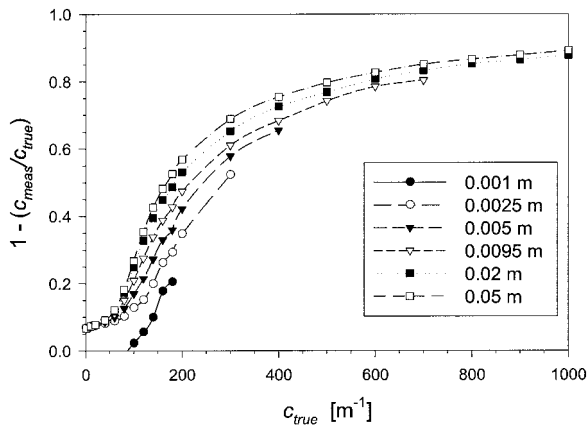


Fig. 6. Measurement error of the beam attenuation for several receiver apertures as indicated by the receiver acceptance radius. The modeled instrument has a path length of 0.1 m, an initial beam radius of 0.001 m, a half-angle of beam divergence of 0.8°, and a half-angle of receiver acceptance of 1.0°. The HG scattering phase function with $g = 0.8$ was used in these calculations.

mean cosine provides a measure of the angular distribution of photons about the main optical axis of the simulated instrument. For $c_{\text{true}} > 400 \text{ m}^{-1}$ the mean cosine changes, slowly approaching its asymptotic value that is somewhat above 0.5. This result confirms that the light field is close to the asymptotic state for $c_{\text{true}} > 400 \text{ m}^{-1}$. However, it must also be noted that the asymptotic mean cosine is a necessary but not a sufficient condition for the existence of the asymptotic light field under arbitrary circumstances.

Designing appropriate instrument geometry, especially determining the size of the collecting surface and the acceptance angle of the receiver, is important for minimizing the measurement error. Figure 6 shows the results of modeling for different sizes of collecting surface (acceptance radii) of the receiver. The HG phase function with $g = 0.8$ was used in these calculations. For an acceptance radius too small to encompass the entire incoming beam (0.001 m) there is an overestimation of measured attenuation (see the lowest curve in Fig. 6 reaching negative values for the relatively small values of c_{true}). This is the result of treating part of the emitted beam as light that is lost owing to scattering. For all the remaining acceptance radii ($\geq 0.0025 \text{ m}$), the measurement underestimates c_{true} over the entire range of c_{true} . The error decreases with decreasing acceptance radius because of a decrease in unwanted scattered light that reaches the receiver. Also, the error curves converge for low c_{true} values that approach 0 as all the radiant power of the source beam hits the collecting area of the receiver, unless the receiver's radius is too small to accommodate the beam. Obviously, the best acceptance radius of the receiver corresponds to the smallest collecting surface that still covers the entire primary (unscattered) beam.

The error of the beam-attenuation measurement also depends strongly on the acceptance angle of the receiver (Fig. 7). For the beam with a half-angle of

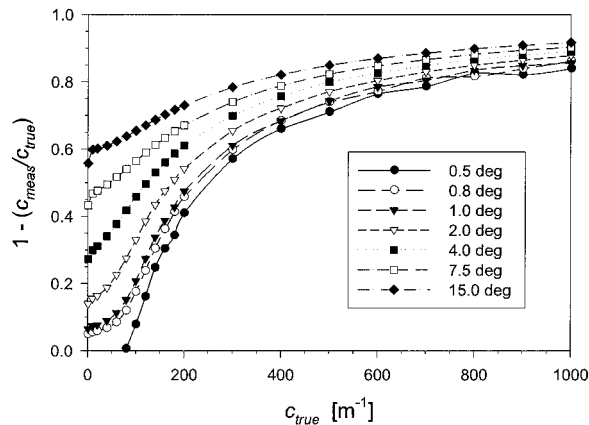


Fig. 7. Measurement error of the beam attenuation for several acceptance angles of the receiver as indicated. The modeled instrument has a path length of 0.1 m, an initial beam radius of 0.001 m, a half-angle of beam divergence of 0.8°, and a receiver radius of 0.0095 m. The HG scattering phase function with $g = 0.8$ was used in these calculations. The curve for the acceptance angle of 0.5° (which is smaller than the beam divergence) is negative for the relatively small values of c_{true} that are due to losses caused by part of the beam's not being accepted by the receiver.

divergence of 0.8°, the use of the receiver with half-angle of acceptance $\theta_a = 0.5^\circ$ results in an overestimation of the measured attenuation. For all the remaining values of θ_a examined, the smaller the acceptance angle, the smaller the measurement error. The best results are achieved with the acceptance angle equal to the beam divergence because then all the unscattered radiation is detected and the amount of unwanted scattered light is minimized. In practice, however, the acceptance angle should probably be slightly larger than the beam divergence to account for possible imperfections in the stability of the beam geometry and mechanical aspects of the instrument.

Figure 8 compares the measurement error of the

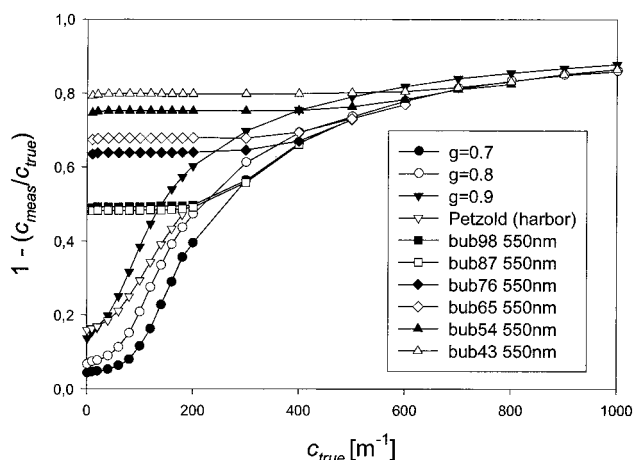


Fig. 8. Comparison of the measurement error of the beam attenuation for all the scattering phase functions considered in this study. The modeled instrument has a path length of 0.1 m, an initial beam radius of 0.001 m, a half-angle of beam divergence of 0.8°, a half-angle of receiver acceptance of 1°, and a receiver radius of 0.0095 m.

Table 1. Relative Forward-Scattering Error Expressed as $1 - c_{\text{meas}}/c_{\text{true}}$ for Various Scattering Phase Functions^a

Phase Function	$1 - c_{\text{meas}}/c_{\text{true}}$	CPF (1.0°)
HG $g = 0.7$	0.0432	0.0474
HG $g = 0.8$	0.0689	0.0768
HG $g = 0.9$	0.148	0.162
Petzold	0.159	0.160
bub98	0.495	0.506
bub87	0.486	0.498
bub76	0.641	0.647
bub65	0.681	0.684
bub54	0.754	0.757
bub43	0.801	0.803

^aThe modeled instrument has a path length of 0.1 m, an initial beam radius of 0.001 m, a half-angle of beam divergence of 0.8°, a half-angle of receiver acceptance of 1°, and a radius of collecting area of 0.0095 m. For comparison, the values of the cumulative phase function (CPF) integrated over the range of scattering angles from 0° to 1° are given. The bubble phase functions are referred to as “bubxy,” where x and y define the void fraction range from 10^{-x} to 10^{-y} .

beam attenuation for all the phase functions considered in this study. At relatively small values of c_{true} , the error is much larger for the bubble phase functions than for the remaining phase functions. For sufficiently small values of c_{true} in the single-scattering regime the error is caused primarily by forward light scattering at angles less than 1°. For higher values of c_{true} , the forward-scattering error is superimposed upon the multiple-scattering error. The multiple-scattering error increases with c_{true} . As a result, for large values of c_{true} the total error is weakly dependent on the type of phase function.

The measurement error caused by forward scattering is quantified by the departure of $1 - c_{\text{meas}}/c_{\text{true}}$ from the value of 0 for small values of true attenuation in the single-scattering regime (the leftmost points in Fig. 3, 4, and 6–8, that satisfy the condition $c_{\text{true}} d < 0.3$). Table 1 summarizes the forward-scattering error for all phase functions. This error results in underestimations of beam attenuation by approximately 4–15% for the HG phase functions, 16% for the Petzold phase function, and 50–80% for the bubble phase functions. These differences are explained by the fact that the proportion of forward scattering at small angles of 0°–1° is much higher for the bubble phase functions than for other phase functions (Fig. 2). Table 1 also shows that the cumulative phase function integrated over the scattering angles of 0°–1° provides a good measure of forward-scattering error.

The major portion of the range of c_{true} considered in this study represents conditions with significant multiple-scattering effects. It is therefore of interest to separate the contributions of forward-scattering error and multiple-scattering error to the total error. One can achieve this separation by appropriately accounting for the forward-scattering error with an alternative definition of the beam-attenuation coefficient. According to this definition, only the scattering that occurs at scattering angles greater

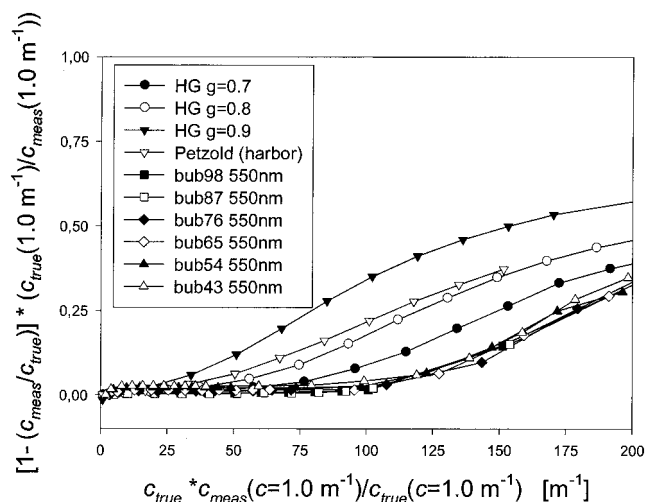


Fig. 9. Multiple-scattering error expressed as a ratio of $1 - c_{\text{meas}}/c_{\text{true}}$ to $c_{\text{meas}}/c_{\text{true}}$ for $c_{\text{true}} = 1 \text{ m}^{-1}$ plotted as a function of c_{true} multiplied by $c_{\text{meas}}/c_{\text{true}}$ for $c_{\text{true}} = 1 \text{ m}^{-1}$. Both variables are subject to multiple scattering after the effects of forward scattering at angles of $<1.0^\circ$ are removed. The relationship is shown for all the phase functions examined in this study. The modeled instrument has a path length of 0.1 m, an initial beam radius of 0.001 m, a half-angle of beam divergence of 0.8°, a half-angle of receiver acceptance of 1°, and a receiver radius of 0.0095 m.

than some small threshold angle contributes to the beam attenuation. Such an alternative beam attenuation, c_{alt} , is smaller than the true beam attenuation by the amount of forward scattering at angles from 0° to the threshold angle. If the threshold scattering angle is appropriately selected to match the half-angle of receiver acceptance, the alternative definition makes it possible to achieve closure between c_{alt} and actual measurements of the beam attenuation.²⁷ Note also that the difference $c_{\text{alt}} - c_{\text{true}}$ represents in effect the forward-scattering error that we are interested in separating from the multiple-scattering error.

Figure 9 shows similar results to those in Fig. 8 with the exception that the effect of the forward-scattering error has been essentially removed. This removal is based on the fact that the multiple-scattering error is negligible in the single-scattering regime, so we can treat the calculated values of $1 - c_{\text{meas}}/c_{\text{true}}$ at sufficiently low values of c_{true} (such as 1.0 m^{-1}) as estimates of the forward-scattering error. Instead of plotting $1 - c_{\text{meas}}/c_{\text{true}}$ versus c_{true} as in previous figures, we show in Fig. 9 the relationship between the variables appropriately modified. Specifically, the vertical axis shows the $1 - c_{\text{meas}}/c_{\text{true}}$ value divided by $c_{\text{meas}}/c_{\text{true}}$ for $c_{\text{true}} = 1 \text{ m}^{-1}$, which represents the multiple-scattering error. The horizontal axis shows the true attenuation c_{true} multiplied by $c_{\text{meas}}/c_{\text{true}}$ for $c_{\text{true}} = 1 \text{ m}^{-1}$, which approximates the alternative beam attenuation, c_{alt} , for the threshold scattering angle of 1.0°. Thus both variables in Fig. 9 are subject to multiple-scattering effects with the forward-scattering effects removed. The normalized ratio of $c_{\text{meas}}/c_{\text{true}}$ approaches 1 at

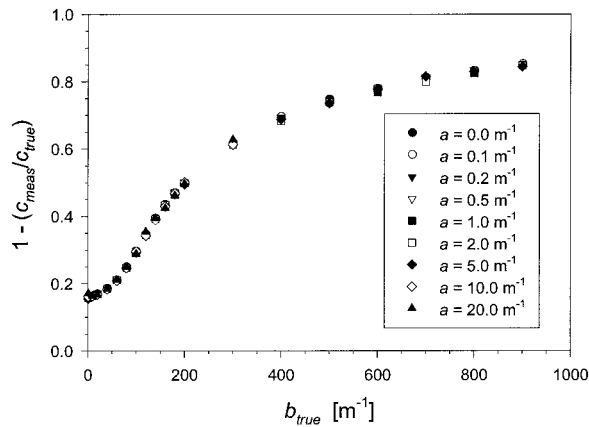


Fig. 10. Measurement error expressed as $1 - c_{\text{meas}}/c_{\text{true}}$ as a function of true scattering coefficient b_{true} for several values of absorption coefficient a , as indicated. An absorption value of as much as $a = 20 \text{ m}^{-1}$ was added with no significant effect on the calculated measurement error. The modeled instrument has a path length of 0.1 m, an initial beam radius of 0.001 m, a half-angle of beam divergence of 0.8° , a half-angle of receiver acceptance of 1° , and a receiver radius of 0.0095 m. The HG scattering phase function with $g = 0.8$ was used in these calculations.

sufficiently low c_{alt} , which indicates that the multiple-scattering error naturally vanishes in the single-scattering regime. At higher values of c_{alt} the multiple-scattering error is similar for all the bubble phase functions examined. The result could be expected because Fig. 1 shows that the bubble phase functions are virtually identical above 1° and because the forward-scattering correction in Fig. 9 accounts for the differences in the phase functions below the scattering angle of 1.0° . However, the differences in the multiple-scattering error are significant if other phase functions are included in the comparison. For example, at $c_{\text{true}} = 100 \text{ m}^{-1}$, multiple scattering results in underestimations of the beam attenuation by 8%, 15%, and 28% for HG phase functions with g values of 0.7, 0.8, and 0.9, respectively. The Petzold phase function has a multiple-scattering error of 11%, whereas the six bubble phase functions have the smallest multiple-scattering error, of less than 3%. Recall, however, that these errors are superimposed upon the forward-scattering error, which was highest for the bubble phase functions and lowest for the HG function with $g = 0.7$ (Table 1).

All the results above were obtained for the medium with a small absorption coefficient corresponding to pure water absorption at 550 nm, which maximized the number of photons reaching the receiver and thus minimized the statistical error of the Monte Carlo simulations. However, increasing the absorption coefficient to 20 m^{-1} does not significantly change the measurement error for the same amount of scattering (Fig. 10). This result should be expected, as the source of both types of measurement error discussed in this paper is scattering. The absorption associated with a potential path length increase owing to scattering does not seem to influence the measurement error. The calculated average path lengths of

photons accepted by the receiver were only minimally affected, even with massive multiple scattering, as long as the beam was thin and the receiver's acceptance angle and acceptance radius were small as in the present simulations. For example, for $b = 100 \text{ m}^{-1}$ and for the typical parameters of the instrument that has a path length of 0.1 m as described above, the relative path length increase for photons detected was less than 0.1% for all the bubble phase functions, 0.5% for the Petzold phase function, and 0.3% for HG phase functions with $g = 0.7$, 0.5% for $g = 0.8$, and 0.6% for $g = 0.9$.

The multiple- and forward-scattering errors are negligible for pure seawater. In pure water the multiple-scattering error would be measurable only for instrument path lengths of the order of tens of meters because the molecular scattering coefficient at visible wavelengths is low. The forward-scattering error is also small because the Rayleigh phase function (a good approximation for pure water) lacks a large forward peak. The fraction of radiant power scattered at small forward angles of 0° – 1° is only 0.00023 of the total scattering coefficient. Our Monte Carlo simulations for the default parameters of the beam transmissometer showed that the relative forward-scattering error for pure water is only 0.034%. This negligible effect makes it possible to use all results of our study in the context of the measurement of the particulate beam-attenuation coefficient in which pure water is used as a reference. In such a context, Φ_0 in Eq. (1) is replaced with Φ_w , which represents the radiant power detected by the instrument in pure seawater. Because forward-scattering and multiple scattering (for an instrument with a typical path length) contribute less than 0.1% to the relative error in c_w of pure water, the error in c_{meas} in Eq. (1) is almost identical, regardless of whether we use Φ_0 or Φ_w .

4. Conclusions

Our three-dimensional Monte Carlo simulations of radiative transfer for the typical geometry of the beam transmissometer used in oceanographic measurements of the beam-attenuation coefficient confirm the generally accepted view that the optimal design of the instrument should have both the acceptance angle and the collecting surface of the receiver as small as possible to accommodate the light beam. The light beam should be as thin and collimated as possible because these beam characteristics determine the extent to which the radius of the collecting surface and the acceptance angle of the receiver can be reduced.

The forward-scattering error associated with the detection of photons scattered at very small angles (generally less than 1°) and the multiple-scattering error associated with the detection of photons scattered more than once along the path length of the instrument are the main sources of error in the measurements of the beam attenuation. One significant challenge for accurate determination of beam attenuation in the ocean is the presence of bubble clouds

entrained into the surface layer by wave breaking. High-density bubble clouds are characterized by high values for the scattering coefficient (and hence the beam attenuation), and the bubble scattering functions are highly peaked in the forward direction. In this study we have determined that, because of forward-scattering error, the typical beam transmissometer with a receiver acceptance half-angle of 1.0° and a path length of 0.1 m will underestimate the beam attenuation by 50–80% (depending on the bubble size distribution and the associated scattering function). Such large errors call for careful correction of the attenuation measurements in the presence of bubble clouds or, alternatively, for the use of an alternative definition of the beam-attenuation coefficient as suggested by Pegau *et al.*²⁷ The multiple-scattering error depends on the magnitude of scattering. For the bubble clouds that have a true beam attenuation of as much as 100 m^{-1} , this error is no more than a few percent.

For the scattering functions that are less peaked in the forward direction than the bubble functions, the forward-scattering error is smaller but the multiple-scattering error is larger. For the Henyey-Greenstein scattering functions with an asymmetry parameter of 0.7–0.9 and the Petzold function from San Diego Harbor (which may represent some assemblages of particles suspended in natural waters), the forward-scattering error is 4–16% and the multiple-scattering error is 8–28% (for a beam attenuation of 100 m^{-1}). However, given the realistic concentrations of particles and the associated magnitude of the beam attenuation (significantly less than 100 m^{-1}) in most natural waters including turbid coastal environments, the multiple-scattering error that is due to particles is expected to be lower than the forward-scattering error that is due to particles.

This study was supported by the U.S. Office of Naval Research Hyperspectral Coastal Ocean Dynamics Experiments (HyCODE) program (grant N00014-02-1-0190).

References

1. R. W. Preisendorfer, "Application of radiative transfer theory to light measurements in the sea," *Union Geod. Geophys. Inst. Monogr.* **10**, 11–30 (1961).
2. C. D. Mobley, *Light and Water: Radiative Transfer in Natural Waters* (Academic, San Diego, Calif., 1994).
3. N. G. Jerlov, *Marine Optics* (Elsevier, Amsterdam, 1976).
4. R. Bartz, J. R. V. Zaneveld, and H. Pak, "A transmissometer for profiling and moored observations in water," in *Ocean Optics V*, M. B. White and R. E. Stevenson, eds., Proc. SPIE **160**, 102–109 (1978).
5. C. Moore, E. J. Bruce, W. S. Pegau, and A. Weidemann, "The WET Labs ac-9: field calibration protocol, deployment techniques, data processing and design improvements," in *Ocean Optics XIII*, S. G. Ackleson, ed., Proc. SPIE **2963**, 725–730 (1996).
6. J. T. O. Kirk, "Monte Carlo modeling of the performance of a reflective tube absorption meter," *Appl. Opt.* **31**, 6463–6468 (1992).
7. K. J. Voss, "Use of the radiance distribution to measure the optical absorption coefficient in the ocean," *Limnol. Oceanogr.* **34**, 1614–1622 (1989).
8. J. R. V. Zaneveld and R. Bartz, "Beam attenuation and absorption meters," in *Ocean Optics VII*, M. A. Blizard, ed., Proc. SPIE **489**, 318–324 (1984).
9. K. J. Voss and R. W. Austin, "Beam attenuation measurement error due to small-angle scattering acceptance," *J. Atmos. Ocean. Technol.* **10**, 113–121 (1993).
10. D. Stramski and J. Tegowski, "Effects of intermittent entrainment of air bubbles by breaking wind waves on ocean reflectance and underwater light field," *J. Geophys. Res.* **106**, 31345–31360 (2001).
11. E. J. Terrill, W. K. Melville, and D. Stramski, "Bubble entrainment by breaking waves and their influence on optical scattering in the upper ocean," *J. Geophys. Res.* **106**, 16815–16823 (2001).
12. X. Zhang, M. Lewis, and B. Johnson, "Influence of bubbles on scattering of light in the ocean," *Appl. Opt.* **37**, 6525–6536 (1998).
13. J. Piskozub, A. R. Weeks, J. N. Schwarz, and I. S. Robinson, "Self-shading of upwelling irradiance for an instrument with sensors on a sidearm," *Appl. Opt.* **39**, 872–1878 (2000).
14. J. Piskozub, P. J. Flatau, and J. R. V. Zaneveld, "Monte Carlo study of the scattering error of a quartz reflective absorption tube," *J. Atmos. Oceanic Technol.* **18**, 438–445 (2001).
15. D. Stramski and J. Piskozub, "Estimation of scattering error in spectrophotometric measurements of light absorption by aquatic particles from three-dimensional radiative transfer simulations," *Appl. Opt.* **42**, 3634–3646 (2003).
16. X. Zhang, M. Lewis, M. Lee, B. Johnson, and G. Korotaev, "The volume scattering function of natural bubble populations," *Limnol. Oceanogr.* **47**, 1273–1282 (2002).
17. C. F. Bohren and D. R. Huffman, *Absorption and Scattering of Light by Small Particles* (Wiley, New York, 1983).
18. E. J. Terrill and W. K. Melville, "A broad-band acoustic technique for measurement of bubble size distributions: laboratory and shallow water measurements," *J. Atmos. Ocean. Technol.* **17**, 220–239 (2000).
19. L. C. Henyey and J. L. Greenstein, "Diffuse radiation in the galaxy," *Astrophys. J.* **93**, 70–83 (1941).
20. T. J. Petzold, "Volume scattering functions for selected ocean waters," SIO Ref. 72–78 (Scripps Institution of Oceanography, La Jolla, Calif., 1972).
21. H. C. van de Hulst, *Light Scattering by Small Particles* (Wiley, New York, 1957).
22. C. D. Mobley, L. K. Sundman, and E. Boss, "Phase function effects on oceanic light fields," *Appl. Opt.* **41**, 1035–1050 (2002).
23. G. W. Kattawar, "A three-parameter analytic phase function for multiple scattering calculations," *J. Quant. Spectrosc. Radiat. Transfer* **15**, 839–849 (1975).
24. V. I. Haltrin, "One-parameter two-term Henyey-Greenstein phase function for light scattering in seawater," *Appl. Opt.* **41**, 1022–1028 (2002).
25. E. J. Terrill, G. Lada, and W. K. Melville, "Surf zone bubble populations," *Acoust. Oceanogr. (Part 2)* **23**, 212–219 (2001).
26. R. M. Pope and E. S. Fry, "Absorption spectrum (380–700 nm) of pure water. 2. Integrating cavity measurements," *Appl. Opt.* **36**, 8710–8723 (1997).
27. W. S. Pegau, J. R. V. Zaneveld, and K. J. Voss, "Toward closure of the inherent optical properties of natural waters," *J. Geophys. Res.* **100**, 13,193–13,199 (1995).